Nano Research

Open Access

Research Article

Conductive MOFs with tailored polarization loss for broadband absorption at ultrathin thickness

Wenqian Zhang[1], Juhua Luo[1] ✉, Jiahuan Shi[1], Bingjie Han[1], Xiangcheng Li[2] ✉, and Yu Xie[3] ✉

[1] *School of Materials Science and Engineering, Yancheng Institute of Technology, Yancheng 224051, China*
[2] *State Key Laboratory of Refractories and Metallurgy, Wuhan University of Science and Technology, Wuhan 430081, China*
[3] *College of Environment and Chemical Engineering, Nanchang Hangkong University, Nanchang 330063, China*

Cite this article: *Nano Research*, **2025**, *18*, 94907919. https://doi.org/10.26599/NR.2025.94907919

ABSTRACT: Conductive metal-organic frameworks (MOFs) have emerged as promising electromagnetic wave absorption (EMWA) properties materials due to their tunable dielectric properties and straightforward synthesis. Nevertheless, achieving broad effective absorption bandwidth (EAB) at ultrathin thickness remains a significant challenge. Herein, a series of rod-haped bimetallic CuM-HHTP (M = Mn, Co, Ni, and Zn) were synthesized via a hydrothermal approach. Remarkably, all fabricated samples demonstrated wide EAB values at ultrathin thickness. The EAB performance was found to correlate positively with the electron transfer capability of metal ions, following the order: CuNi > CuCo > CuZn > CuMn. This trend can be attributed to subtle variations in charge carrier concentrations and dipole moment modifications induced by the coordination of heterogeneous metal ions to hydroxyl groups, which arise from the coordination tendency and bond strength of the heterobimetallic binding to the ligands. The EAB value of CuNi-HHTP reached up to 7.12 GHz (10.88–18.00 GHz) at a matching thickness of only 1.78 mm. The outstanding EMWA performance was originated from optimized impedance matching, synergistic dipole and defect polarization, interface polarization, and conductive loss. Additionally, radar cross-section simulation confirmed the material's practical applicability in EMWA. This study presents a novel strategy for designing high-performance bimetallic conductive MOFs absorbers with tailored electromagnetic properties.

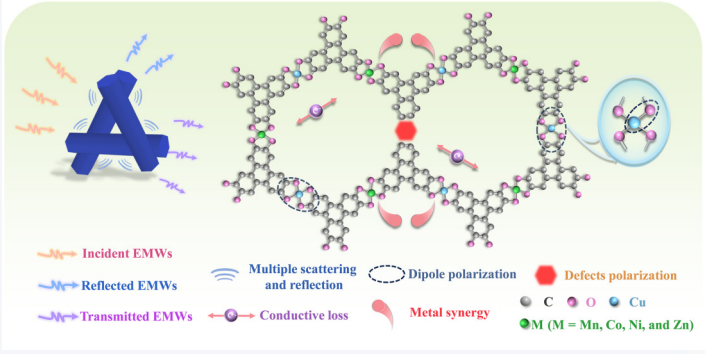

KEYWORDS: bimetallic conductive metal-organic frameworks (MOFs), electromagnetic wave absorption (EMWA), wide-bandwidth, polarization loss

1 Introduction

The rapid development of electronic devices and communication technologies has led to the widespread utilization of electromagnetic wave (EMW) in modern society. However, the electromagnetic pollution has brought about potential threats to both human health and environmental sustainability. In military applications, electromagnetic interference can severely disrupt radar systems and communication devices, compromising operational effectiveness [1–3]. To mitigate these challenges, significant research efforts have been directed toward designing high-efficient EMW absorbing (EMWA) materials with optimal characteristics, including thin thickness, wide bandwidth, light weight, and strong absorption capabilities [4–6]. Conventional EMWA materials, including magnetic materials (such as ferrites [7] and magnetic metals [8]), carbon-based materials (e.g., graphene [9] and carbon nanotubes [10]), and ceramics [11] and their composites, have been extensively employed. Nevertheless, their practical applications are often hindered by intrinsic limitations, including poor absorption bandwidth and inadequate absorption intensity. These shortcomings underscore the pressing demand for innovative EMWA materials with enhanced performance.

Metal-organic frameworks (MOFs) are crystalline porous materials constructed by inorganic metal nodes bridged by organic ligands [12]. Owing to their exceptional features such as large specific surface area, well-defined porosity, diverse topologies, and

Received: June 8, 2025; **Revised:** August 5, 2025
Accepted: August 13, 2025

✉Address correspondence to Juhua Luo, ljh@ycit.edu.cn; Xiangcheng Li, lixiangcheng@wust.edu.cn; Yu Xie, xieyu_121@163.com

tunable structural units, MOFs have garnered widespread applications in various fields including catalysis [13], supercapacitors [14], energy storage [15], sensors [16], and EMWA [17–19], etc. However, their limited electrical conductivity and structural collapse upon high-temperature carbonization significantly impair their EMWA performance [20, 21]. In this context, the conductive MOFs have emerged as promising EMWA materials [12]. These materials offer three key advantages. 1) They maintain the original morphology without requiring high-temperature calcination. 2) They exhibit enhanced electron mobility for improved conducive loss [22]. 3) The rich functional groups within the ligands enable strong polarization loss through coordination with transition metals [23]. The aromatic functional ligands employed in conductive MOFs primarily include: 1) polycarboxylic acid ligands (e.g., BTC), 2) polyhydroxy aromatic ligands (e.g., HHTP), and 3) sulfurcontaining ligands (e.g., TTFTB) [24]. Particularly, the HHTP ligand possesses abundant functional groups and outstanding thermal stability. Moreover, its extended conjugated π-system, with an intrinsic π–π conjugation system, facilitates efficient electron transport and readily forms porous frame-works through metal coordination [25]. Notably, the conductive MOFs based on HHTP ligands represent ideal candidates for EMWA materials. For instance, Shan et al. demonstrated the $Cu_3(HHTP)_2$ achieving a minimum reflection loss (RL_{min}) value of −56.45 dB and the effective absorption bandwidth (EAB, RL < −10 dB) value of 5.76 GHz at the thicknesses of 2.00 mm [12]. This work marked the first application of conductive MOFs in the field of EMWA through a simple and influential strategy. However, due to monometallic conductive MOFs, suffer from limited tunability in EMWA performance. To further enhance EMWA performance, Qu et al. developed bimetallic Co/Cu conductive MOFs achieving an RL_{min} value of −61.00 dB at a thickness of 2.26 mm [26]. The absorption performance was significantly enhanced by modulating the metal ion ratio, highlighting the promise of bimetallic systems. Nevertheless, the fundamental relationship between bimetallic composition and EAB modulation remains unclear, presenting a critical research gap.

In this work, we successfully prepared a series of CuM-HHTP (M = Mn, Co, Ni, and Zn) bimetallic MOFs using a modified one-step hydrothermal method. The study was conducted in two phases: First, Zn^{2+} was gradually incorporated into a Cu-based system to systematically evaluate the effects of varying Cu^{2+}/Zn^{2+} ratios on electromagnetic properties. Subsequently, we explored the influence of different metal ions (Mn^{2+}, Co^{2+}, and Ni^{2+}) substituted at the optimal ratio on dielectric loss modulation. Guided by Hund's rule and the Pauli exclusion principle, we observed that the distinct electron donation and acceptance abilities of these transition metals significantly modulated electron transfer capabilities, thereby engineering polarization loss characteristics. This atomic-level control strategy allows for precise compositional optimization to tailor EMWA performance. Notably, the exceptional EAB performance originates from the delicate equilibrium between attenuation performance and impedance matching, enhances EMWA capability. Concurrently, the synergistic impact of the bimetallic system, π–π interactions induced by charge transfer, and anisotropy of the interlayer structure provide absorption sites for EMW, promoting multiple scattering and reflections that further enhance EMWA. The results indicate that CuNi-6 achieves an EAB value of 7.12 GHz (10.88–18.00 GHz) at a matching thickness of only 1.78 mm. Additionally, for the CuZn-1, the RL_{min} value reaches −66.20 dB at 3.24 mm matching thickness at a frequency of 7.44 GHz. This innovative strategy of composition-tunable MOFs establishes a versatile platform for designing next-generation EMWA materials.

2 Experimental

Synthesis of the CuM-HHTP: A series of bimetallic conducting MOFs were prepared by a hydrothermal method. The samples were first prepared by control-ling different molar ratios of Cu^{2+}, Zn^{2+} (2:1, 1:1, and 1:2) with the ligand HHTP noted as CuZn-*X* (*X* = 1, 2, and 3). Sample CuM-*Y* (M = Mn, Co, and Ni; *Y* = 4, 5, and 6) was obtained by replacing the Zn^{2+} element with M^{2+} (M = Mn, Co, and Ni). The Electronic Supplementary Material (ESM) contains details of the synthesis process, characterization and test methods for all final products.

3 Results and discussion

3.1 The composition, morphology, and microstructure of CuM-HHTP

Figure 1(a) illustrates the synthesis process of the rod-shaped CuM-HHTP (M = Mn, Co, Ni, and Zn) via a hydrothermal method. Following a previously reported procedure [27], equimolar amounts of $(CH_3COO)_2Cu{\cdot}H_2O$, $(CH_3COO)_2M{\cdot}4H_2O$, and HHTP underwent a coordination reaction to form conductive CuM-HHTP nanostructures. During the hydrothermal process, the –OH groups of the HHTP coordinated with Cu^{2+} and M^{2+} ions to construct a planar structure featuring hexagonal pores [28]. These planar structures subsequently assembled via π–π stacking into uniform rod-like morphologies, where numerous benzene rings established an extended π-conjugated structure and three-dimensional conductive network throughout MOFs crystals. Notably, HHTP features multiple functional groups that readily coordinate with transition metal ions, generating a layered π–π conjugated system [29]. The resulting π–π interactions not only directed ensured planar growth but also guided longitudinal stacking of the conductive MOFs [30]. Structurally, each metal node bridged two adjacent HHTP ligands forming interconnected π stacking and conjugated networks, that collectively enhanced conductivity for optimized EMWA performance [31].

X-ray diffraction analysis of the CuM-HHTP (M = Mn, Co, Ni, and Zn) are presented in Fig. 1(b). All samples exhibited characteristic peaks at 9.5°, 12.7°, and 27.6°, indexed to the (200), (201), and (002) crystalline planes, respectively, in good agreement with previous literature reports [22]. The observed diffraction peaks at 9.5° and 12.7° confirm a hexagonal layer structure oriented along the ab plane for the CuM-HHTP. Furthermore, the strong diffraction peak at 27.6° verifies the preferred longitudinal assembly of rod-like structures within the sample [32]. Notably, all samples displayed well-defined diffraction peaks without detectable impurity phases, demonstrating a high level of crystallinity in the prepared samples. Comparative analysis revealed that CuZn-*X* and CuM-*Y* showed enhanced peak intensity at an angle of 27.6° relative to other samples, suggesting their highest degree of longitudinal stacking crystallinity realized among all investigated compositions examined in this study [33]. This combination of crystallinity and structural integrity promotes efficient electron transport processes

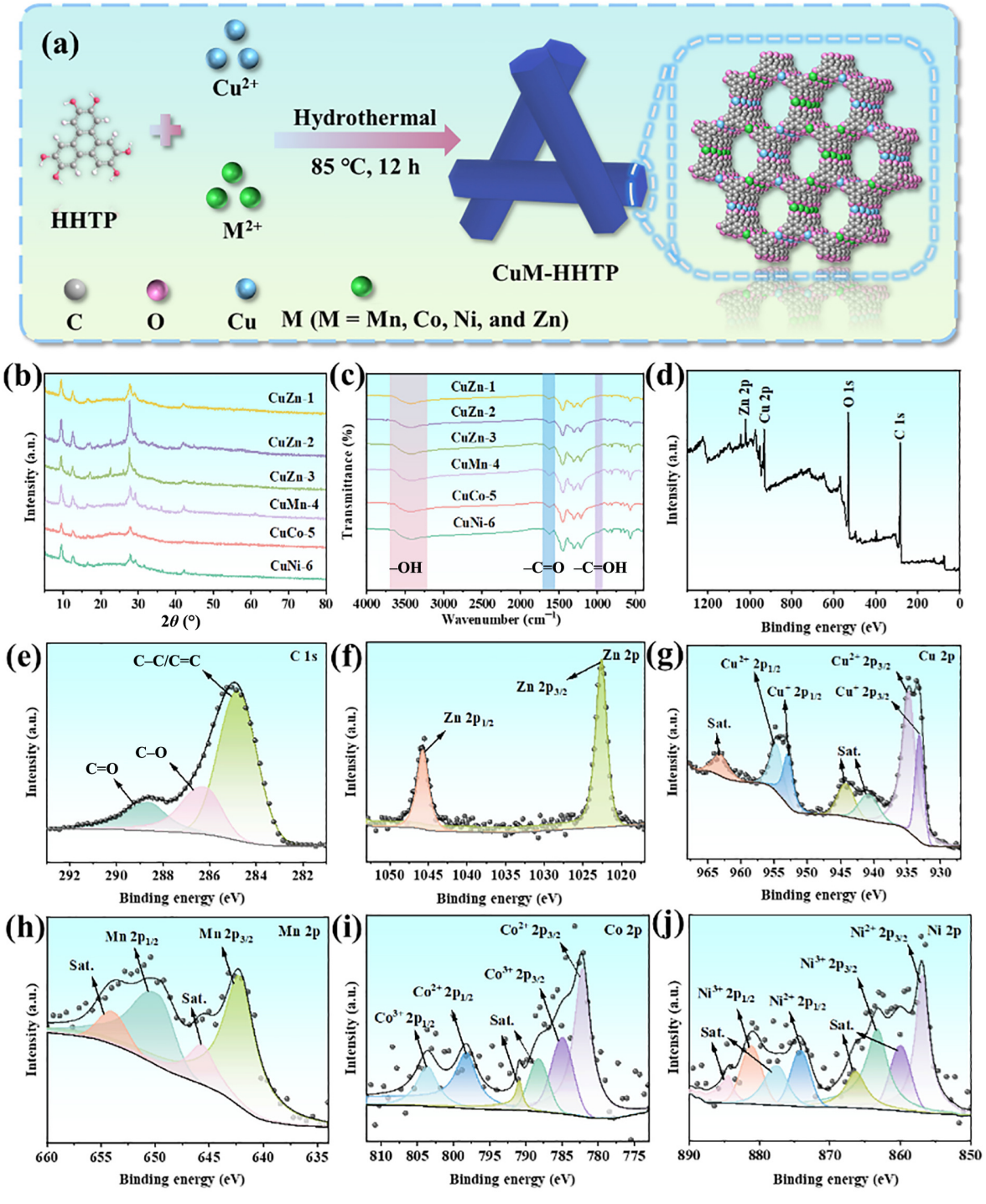

Figure 1 (a) Schematic illustration of the preparation process of the CuM-HHTP (M = Mn, Co, Ni, and Zn). (b) XRD patterns of all samples. (c) FT-IR spectra of all samples. XPS spectra of the CuZn-1: (d) full spectrum, (e) C 1s, (f) Zn 2p, and (g) Cu 2p. XPS spectra of the CuM-*Y*: (h) Mn 2p, (i) Co 2p, and (j) Ni 2p.

thereby enhancing both electrical conductivity and ultimately improving EMWA performance.

FT-IR analysis, as shown in Fig. 1(c), confirmed identical functional groups across all samples. The characteristic peaks observed at wavenumbers of 3430 and 990 cm^{-1} are attributed to the stretching vibrations of –OH and –C–OH in HHTP, respectively [26]. Notably, the appearance of –C=O vibrational peak at 1633 cm^{-1} indicates partial oxidation of ligands during synthesis to achieve charge equilibrium [30]. Furthermore, the weak absorption band at 530 cm^{-1} confirms the formation of metal-oxygen coordination bonds coordination bonds [30].

XPS characterization using the CuZn-1 as a representative example, the survey spectrum (Fig.1(d)) confirmed the presence of C, O, Cu, and Zn elements. Figure 1(d) displays the total C and metal ion spectra. The XPS spectrum of C 1s in Fig. 1(e) categorizes into three peaks at 284.80, 286.19, and 288.59 eV, corresponding to the C–C/C=C, C–O, and C=O bonds [34], respectively. The dominant C–C/C=C signal reflects the abundance of benzene rings

present in the CuZn-1, which significantly contribute to their excellent electrical conductivity and enhance EMWA performance. In the Zn 2p region (Fig. 1(f)), 1022.57 and 1045.69 eV were assigned to Zn $2p_{1/2}$ and Zn $2p_{3/2}$, respectively [12], while those at 934.76 and 954.60 eV in Fig. 1(g) correspond to Cu^{2+} binding energies for their respective spin-orbit components (Cu^{2+} $2p_{1/2}$ and Cu^{2+} $2p_{3/2}$) [12]. The peaks at 933.14 and 952.82 eV are assigned to Cu^{+} $2p_{1/2}$ and Cu^{+} $2p_{3/2}$, respectively [22]. Additionally, the small peaks at 940.75 and 944.17 eV are related to the satellite peaks of Cu $2p_{3/2}$, while the small peak at 963.00 eV belong to the satellite peak of Cu $2p_{1/2}$ [22]. Furthermore, Figs. 1(h)–1(j) present the XPS spectra of Mn 2p, Co 2p, and Ni 2p in the CuM-Y, samples [31, 33], with other samples shown in the supporting information (Figs. S1(i) and S1(j) in ESM). The binding energy of Cu varied slightly for all samples in XPS, resulting from the different charge transfer abilities of metal ions. Collectively, both XPS and FT-IR analyses confirm the successful formation of CuM-HHTP materials.

Nitrogen adsorption–desorption analysis in Fig. S2 in the ESM revealed typical type-IV isotherm, confirming the presence of the mesoporous structure [5]. Quantitative data are summarized in Table S1 in the ESM. The Brunauer–Emmett–Teller (BET) for CuM-HHTP (M = Mn, Co, Ni, and Zn) are calculated to be 228.56, 189.17, 169.23, 160.66, 187.84, and 209.99 $m^2 \cdot g^{-1}$, respectively. With corresponding pore volume (V_{pore}) values are 0.51, 0.44, 0.45, 0.35, 0.36, and 0.40 $m^3 \cdot g^{-1}$, respectively. According to the Maxwell-Garnett theory, larger specific surface area provides the EMWA sites and improve the electron transfer rate, while the porous structure simultaneously reduce the complex dielectric constant and enhances the impedance matching [5]. Notably, the mean pore size (D_{pore}) values for CuZn-2, CuMn-4, CuCo-5 and CuNi-6 are comparable at 11.71, 12.74, 12.36, and 12.08 nm, respectively. These structural features collectively enhance multiple scattering and reflections of the incident EMW through interfacial polarization [8]. Moreover, the porous structure not only reduce material weight but also contribute to superior EMWA performance.

Morphological characterization of CuZn-1, CuZn-2, CuZn-3, CuMn-4, CuCo-5, and CuNi-6 was performed using SEM (Figs. 2(a)–2(f)). All samples exhibited well-defined rod-like

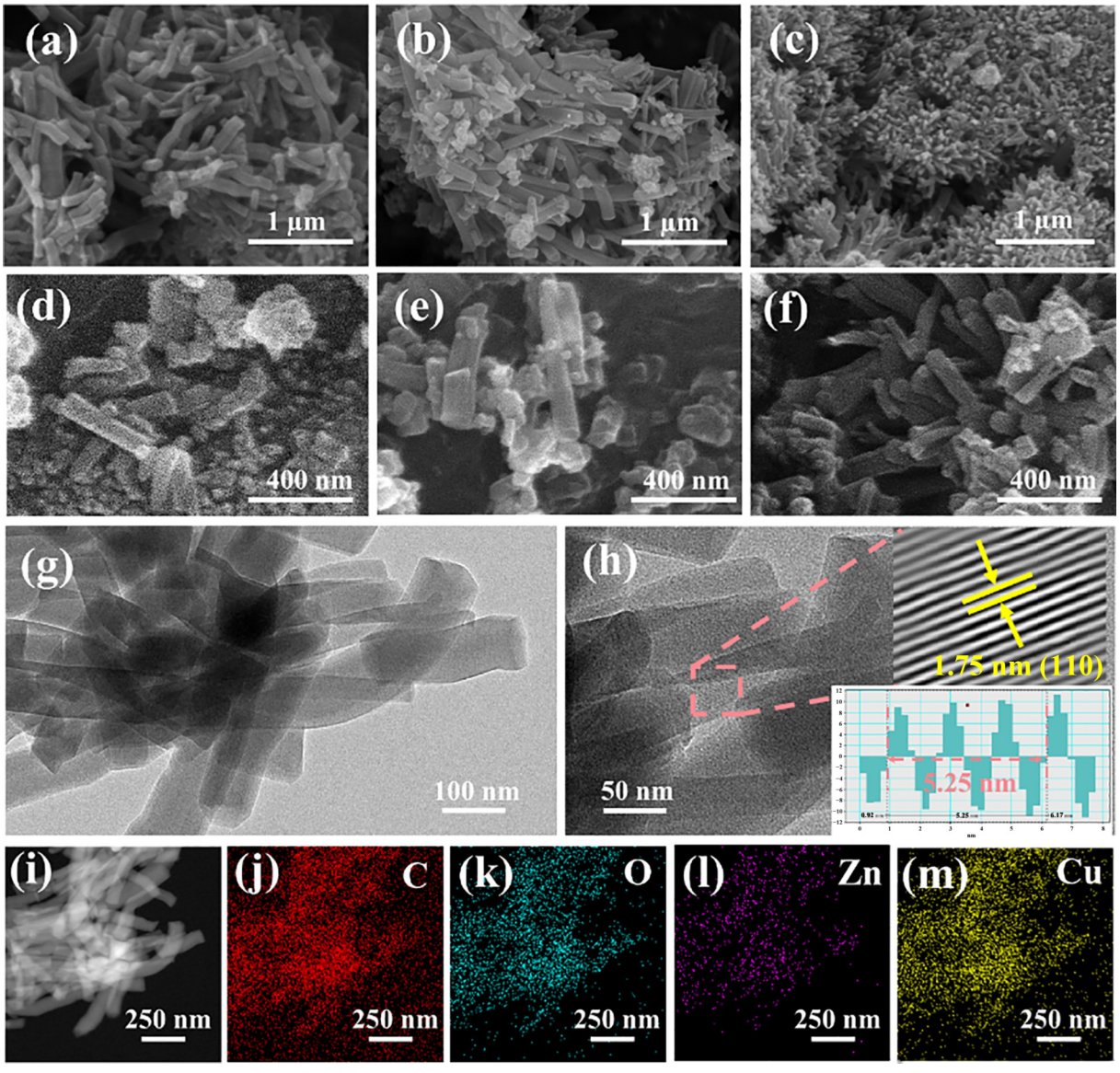

Figure 2 SEM images of (a) CuZn-1, (b) CuZn-2, (c) CuZn-3, (d) CuMn-4, (e) CuCo-5, and (f) CuNi-6. (g) and (h) HRTEM images, and (i)–(m) TEM-EDS elemental mapping images of CuZn-1.

morphologies, confirming that bimetallic composition variation preserves the morphology with slight nanorod aggregation observed, attributed to the high surface energy characteristic of nanoscale bimetallic conductive MOFs promoting aggregation of nanoparticles through mutual attraction. Notably, Figs. 2(a)–2(c) reveals that CuZn-1 displays uniform size distribution and good dispersion, which maximizes EMWA active sites for enhanced performance. As can be seen from Figs. 2(a)–2(f), there is no significant change in rod diameter and size for all samples. This observation suggests that changing the metal ions does not have a significant outcome on the size change, thus indicating that EMWA performance is not significantly affected by morphology. The structure of HHTP incorporates numerous groups bound to transition metal ions to form a layered π–π conjugated system. The two-dimensional laminar structure aligns longitudinally, promoting the formation of rod-like samples. In this scenario, the robust π–π interaction ensure planar growth and longitudinal stacking of conductive MOFs. A network with π-stacking and π-conjugate network is established between adjacent HHTP ligands centered on one metal in each stratum, which enhances conductivity while facilitating EMWA through increased the conductive loss. Furthermore, these 1D nanostructures promote multiple scattering and reflections of EMW, while their shape anisotropy EMWA capacity [35]. The intrinsic shape anisotropy of these 2D-derived nanorods contributes to EMWA performance by generating localized EMWA sites under electromagnetic excitation [36].

Advanced microstructural characterization was conducted using transmission electron microscopy (TEM) and high-resolution TEM (HRTEM), as depicted in Figs. 2(g)–2(m). The well-defined rod-like morphology of the CuZn-1 is clearly shown with an average diameter of about 100 nm and a stack length of 1 μm (Fig. 2(g)). Additionally, from Fig. 2(h), lattice fringe distances of 1.75 nm were observed, corresponding to the diameter of a hexagonal pore formed by the metal ion and ligand in the conductive MOF. Elemental distribution analysis (Figs. 2(i)–2(m)) confirmed uniform dispersion of elements C, O, Cu, and Zn throughout the architecture. The C and O elements originate from organic ligands while Cu and Zn are de-rived from inorganic metal salts. Notably, successful preparation of bimetallic conductive MOFs is unambiguously demonstrated by copper and zinc co-distribution.

3.2 EMWA performance of the CuM-HHTP

The electromagnetic parameters were characterized from 2.00–18.00 GHz using a vector network analyzer. Based on the transmission line theory, the EMWA properties are quantified by a reflection loss (RL) using Eqs. (1) and (2) [37, 38]

$$\mathrm{RL} = 20\lg\left|\frac{Z_{\mathrm{in}} - Z_0}{Z_{\mathrm{in}} + Z_0}\right| \quad (1)$$

$$Z_{\mathrm{in}} = Z_0\sqrt{\frac{\mu_{\mathrm{r}}}{\varepsilon_{\mathrm{r}}}}\tanh\left(\mathrm{j}\frac{2\pi f d\sqrt{\mu_{\mathrm{r}}\varepsilon_{\mathrm{r}}}}{c}\right) \quad (2)$$

where Z_{in} represents the input impedance of the sample, Z_0 denotes the free-space impedance of the sample. The $\mu_r = \mu' - \mathrm{j}\mu''$ and $\varepsilon_r = \varepsilon' - \mathrm{j}\varepsilon''$ are the relative complex permeability and the relative complex permittivity, respectively. Additionally, d represents the thickness of the coating of the sample, f denotes the frequency of the EMW, and c symbolizes the speed of light in vacuum. Typically, when the value of the sample RL falls below −10 dB, it signifies that 90% of the EMW is absorbed [39, 40]. Optimal EMWA performance requires both strong absorption and broad bandwidth [1]. Figures 3(a1)–3(c3) present the 2D and 3D plots, illustrating the RL values at different thicknesses for the CuZn-X with various ratios. In Figs. 3(a1)–3(a3), the CuZn-1 demonstrates an $\mathrm{RL_{min}}$ value of −66.20 dB at 7.44 GHz with a matching thickness of 3.24 mm. However, when the matching thickness is 2.00 mm, the EAB value reaches 4.88 GHz (13.12–18.00 GHz). The CuZn-2 (Figs. 3(b1)–3(b3)) exhibits an EAB value of 6.16 GHz (11.84–18.00 GHz) at 2.29 mm and an $\mathrm{RL_{min}}$ value of −27.55 dB at 2.55 mm. As for the CuZn-3, it can be viewed clearly from Figs. 3(c1)–3(c3) that the $\mathrm{RL_{min}}$ value is −14.90 dB and the EAB value is 3.12 GHz (7.52–10.64 GHz) at a matching thickness of 4.00 mm. Notably, the CuZn-1 exhibited the strongest RL value, suggesting excessive Zn^{2+} impede electron migration in conductive MOFs, reducing EMW loss [12]. Fascinatingly, the EAB shows a distinct non-monotonic trend with increasing Cu^{2+} incorporation. The phenomenon can be attributed to the synergistic effect of the bimetallic system, where the coexistence of Zn^{2+} and Cu^{2+} enhances electron transfer, thereby significantly improving the EMWA performance [23]. However, an excessive Cu^{2+} content compromises broad-band absorption. To elucidate the relationship between the EAB value and bimetallic composition in the samples, the resulting CuM-*Y* (M = Mn, Co, and Ni) samples are prepared, and their EAB and $\mathrm{RL_{min}}$ values at different thicknesses are systematically studied and evaluated. Figures 3(d1)–3(f3) depict the 2D and 3D RL profiles of the CuM-*Y* at different thickness. The CuMn-4 demonstrates an EAB value of 6.00 GHz (12.00–18.00 GHz) at a matching thickness of 1.83 mm (Figs. 3(d1)–3(d3)). The CuCo-5 shows an EAB value of 6.48 GHz (10.96-17.44 GHz) at 1.76 mm (Figs. 3(e1)–3(e3)). The CuNi-6 exhibits the EAB value of 7.12 GHz (10.88-18.00 GHz) at a matching thickness of only 1.78 mm, covering the entire Ku-band and part of the X-band (Figs. 3(f1)–3(f3)). Remarkably, all samples demonstrate broadband absorption capabilities at thin matching thicknesses. Nonetheless, the performance discrepancies are observed among the samples with distinct metal ions. The order for EAB characterization is as follows: CuNi-6 > CuCo-5 > CuZn-2 > CuMn-4, which is inextricably linked to the synergistic effect of the bimetals [23]. Consistent with Hund's rule and the Pauli exclusion principle, the electron donation capacity follows: Ni > Co > Zn > Mn [41], directly correlating with their EAB performance. Based on this phenomenon, the analysis reveals that the varying abilities of different elemental ions to donate and accept electrons result in different charge transfer capabilities between metals and ligands [41]. The variation in dipole moments induced by the coordination tendencies and bond strengths of heterobimetallic ions with hydroxyl ligands. This leads to differences in dipolar polarization abilities, consequently affecting the EMWA capabilities of the synthesized samples. Stronger electron donating ability leads to more intense dipole polarization between metal and ligand, and the sample with more unpaired electrons typically exhibits better conductivity, resulting in stronger EMW loss capability. These findings highlight the potential for composition-tuned the materials for wideband absorption.

In summary, based on the variation in EMWA persuasively across all samples, it is evident that the absorption peak systematically shifts towards lower frequencies with an increase in the matching thickness of the sample, as governed by the quarter wavelength model (Eq. (3)) [9, 42]

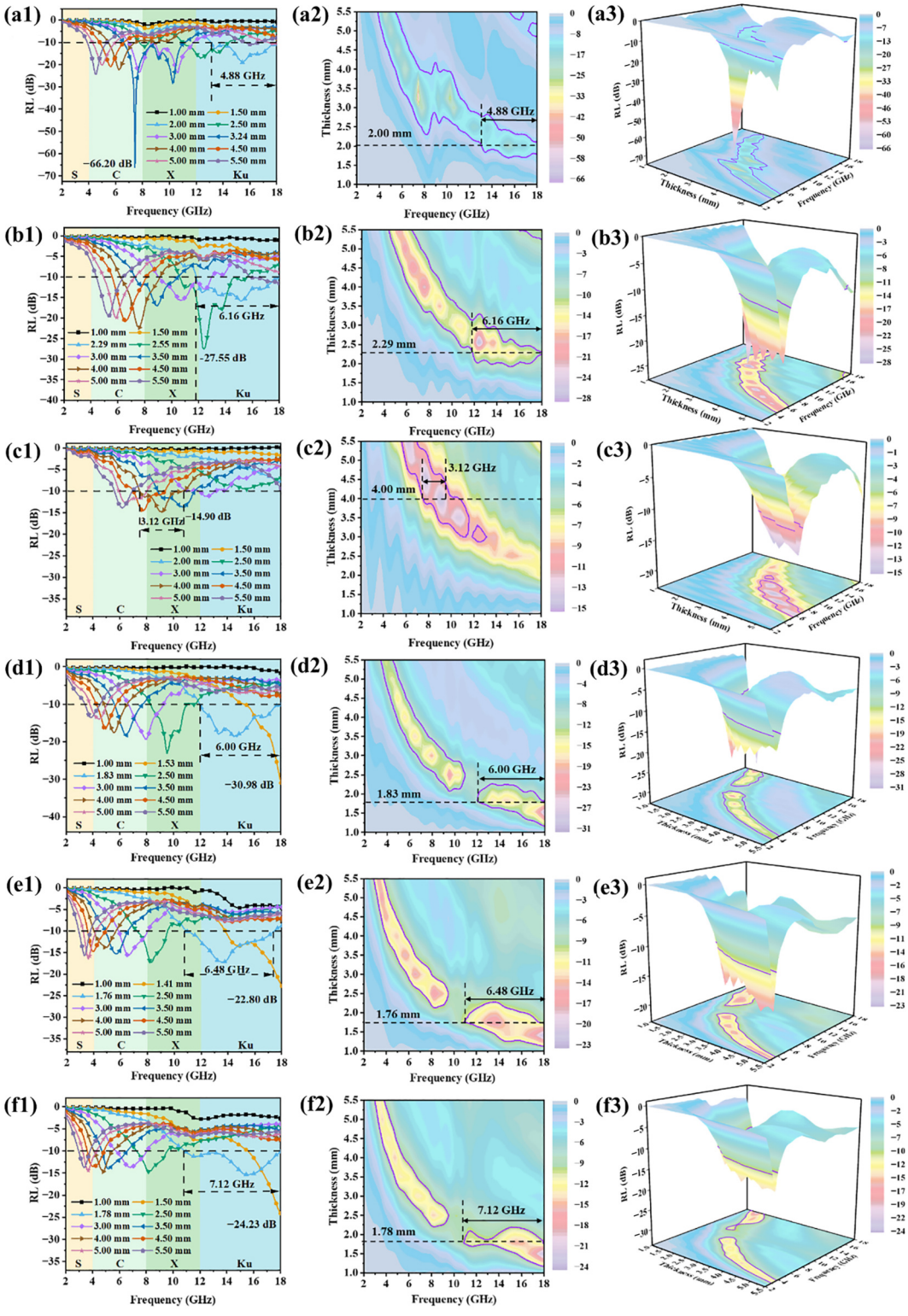

Figure 3 The 2D and 3D plots of (a1)–(a3) CuZn-1, (b1)–(b3) CuZn-2, (c1)–(c3) CuZn-3, (d1)–(d3) CuMn-4, (e1)–(e3) CuCo-5, and (f1)–(f3) CuNi-6.

$$t_m = \frac{nc}{4f_m \mathrm{Re}\sqrt{|\varepsilon_r||\mu_r|}} \quad (n = 1, 3, 5, \ldots) \tag{3}$$

where the n denotes the mode number, the Re represents the real part of the complex value, the t_m is the matching thickness of material, and f_m corresponds to the peak frequency. From the above Eq. (3), it is recognized that the matching thickness is inversely proportional to the corresponding frequency. Figure S3 in the ESM illustrates the quarter wavelength theory plots for all samples, demonstrating their adherence to the quarter wavelength theory and exhibiting phase cancellation of EMW at the air-sample interface when both t_m and f_m of the sample satisfy the aforementioned equation [43].

As the conductive MOFs primarily function as dielectric

materials, we focus on the ε_r characteristics of the samples. The real part (ε') and imaginary part (ε'') components of the complex dielectric constant represent the storage and dissipation capacities of the EMW energy, respectively [44]. The ratio of the real and imaginary parts of the complex dielectric permittivity represents the dielectric loss tangent ($\tan\delta_\varepsilon$). Consequently, the $\tan\delta_\varepsilon$ serves as a critical parameter for assessing dielectric loss and determining EMWA properties [6]. Frequency-dependent variations of ε' and ε'' for the samples are presented in Figs. 4(a) and 4(b), revealing a direct correlation between the electron gain and loss capabilities of metal ions and the dielectric parameters in different types of conductive MOFs. As illustrated in Fig. 4(a), the ε' values for CuZn-1, CuZn-2, and CuZn-3 diminished from 9.83 to 6.33, 7.95 to 5.20, and 6.32 to 4.73, respectively. This could be attributed to the frequency dispersion effect of the sample under the action of alternating electromagnetic fields [45]. Notably, the proportion of Cu ions increases, the samples exhibit higher ε' values. Figure 4(b) shows fluctuations in ε'' values across frequency, indicating the existence of multiple polarization phenomena [46]. The CuZn-2 demonstrates the highest values of both ε' and ε'', highlighting that a Cu:Zn ratio of 2:1 optimizes dielectric storage and dissipation capabilities [44]. The results demonstrate precise bimetallic element ratio can control the electromagnetic parameters and change the EMWA performance. Notably, the CuM-*Y* samples prepared by changing the bimetallic species possess higher ε' values, while all the tractions show a decreasing trend due to the polarization lagging behind the frequency of the EMW [45]. Specifically, ε' initially ranges from 14.58 to 6.59, 16.63 to 8.30, and 15.53 to 7.22, respectively, illustrating that adjusting the bimetallic fraction enhances dielectric storage capacity in these samples. All samples

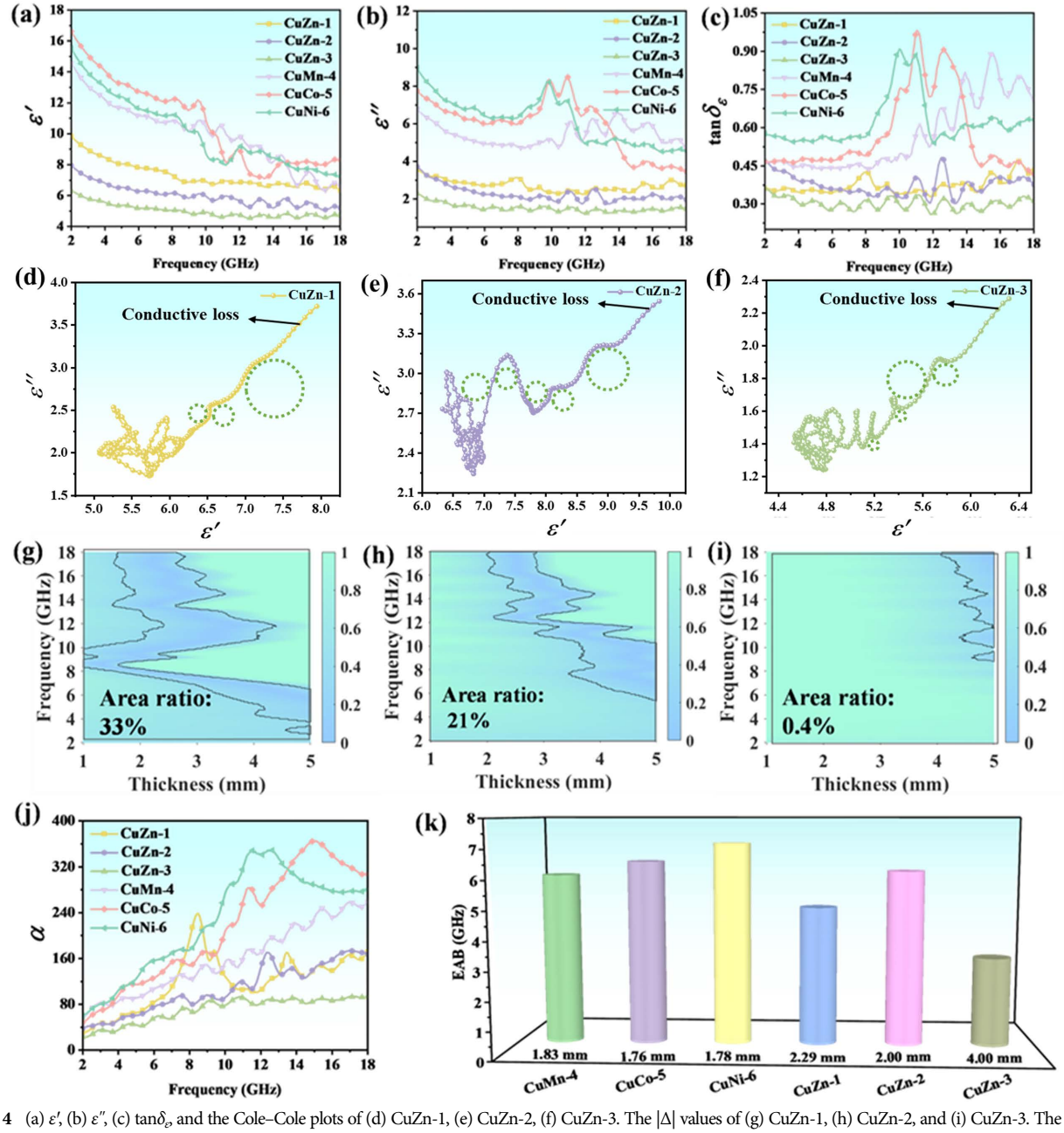

Figure 4 (a) ε', (b) ε'', (c) $\tan\delta_\varepsilon$, and the Cole–Cole plots of (d) CuZn-1, (e) CuZn-2, (f) CuZn-3. The $|\Delta|$ values of (g) CuZn-1, (h) CuZn-2, and (i) CuZn-3. The α values of (j) CuM-HHTP (M = Mn, Co, Ni, and Zn) and (k) Opti-mal EAB bar charts for different samples.

consistently shows slight fluctuations after tracking frequencies above 8.00 GHz. Meanwhile, Fig. 4(b) demonstrates that all ε'' values of CuM-*Y* display vibrational peaks attributed to dielectric material polarization relaxation contributing significantly to dielectric loss [47]. Therefore, modulating electromagnetic parameters by varying the different metals is feasible. The tangent values of the dielectric loss of CuZn-*X* with different ratios are displayed in Fig. 4(c). It can be seen that the tan δ_ε values for CuZn-*X* fall within the range of 0.25–0.5. Among them, the CuZn-1 exhibits the highest values in the frequency bands of 6.56–10.48, 14.72–15.76, and 16.48–18.00 GHz, where its dielectric loss significantly contributes to performance enhancement [6]. The CuZn-2 possesses a relatively high value of tanδ_ε in the high-frequency band consistent with its EAB range. Clearly, the sample exhibits a broad EAB value. Similarly, all the CuM-HHTP (M = Mn, Co, and Ni) samples have higher tanδ_ε values within the corresponding EAB range. It is further emphasized that precise adjustment of the ratio and components of the bimetallic is crucial for achieving desirable EMWA properties. In addition, due to the incorporation of bimetallic, there are an improvement in the magnetic properties. Although the magnetic property remain relatively weak but cannot be disregarded. Figure S4 in the ESM gives the real part of the permeability of the samples (μ'), the imaginary part of the permeability (μ''), and the variation curves of the complex permeability and magnetic loss tangent (tanδ_μ) curves for each sample. The μ' and μ'' values of CuZn-X and CuMn-4 both remain approximately constant at 1 and 0, respectively, while CuCo-5 and CuNi-6 display significant fluctuations in both μ' and μ'' values owing to the synergistic impact induced by bimetals. Negative values observed for μ'' can be owing to internal charge movement generating alternating electric field which subsequently creates internal magnetic field, excess magnetic energy is radiated when these internal magnetic field surpasses original ones, multiple fluctuation peaks seen in waveform are a result of natural resonance at low frequencies as well as exchange resonance at high frequencies [48]. From Fig. 4(c) and Fig. S5 in the ESM, it becomes apparent that tan δ_μ values for all samples are lower than tanδ_ε values, inferring that dielectric loss remains as predominant governing EMW loss.

The dielectric loss of dielectric materials comprises conductive loss and polarization loss, which can be characterized using Debye relaxation theory [10, 49]. The Cole–Cole relationship between ε' and ε'', is expressed as Eq. (4)

$$\left(\varepsilon' - \frac{\varepsilon_s + \varepsilon_\infty}{2}\right)^2 + (\varepsilon'')^2 = \left(\frac{\varepsilon_s - \varepsilon_\infty}{2}\right)^2 \quad (4)$$

where ε_s and ε_∞ denote the static dielectric constant and there lative dielectric constant at the high-frequency limit, respectively. Polarization loss can be elucidated by the Debye relaxation theory, the Cole–Cole semicircles obtained from the depiction of ε' and ε'' represent individual process of Debye relaxation [50]. Figures 4(d)–4(f) displays the Cole–Cole plots of CuZn-*X* samples. Multiple irregular semicircles appear in all samples, clearly indicating several polarization relaxation processes occurring within the samples. The Cole–Cole plots of CuM-*Y* reveal multiple semicircles in the same region (Fig. S5 in the ESM), indicating significant contributions from polarization loss. These distorted semicircles reflect various dielectric loss mechanisms, with dipole polarization caused by electron transfer between metal ions and functional groups being the most prominent. As the curves evolve, the Cole–Cole plots ultimately transform into a straight line, at which point conductive loss becomes the primary loss mechanism of the samples [51]. Concurrently, the Cole–Cole plots of ε' and ε'' reveal linear behavior in the low-frequency range for all samples, confirming the dominance of conductive loss at these frequencies. The CuM-*Y* samples possess high dielectric constants, indicating that conductive loss predominates at low frequencies. This explains their absorption capability in the low-frequency range and further suggests that conductive loss primarily controls EMWA in this band. The presence of noncovalently bonded organic segments, such as π–π stacking, facilitates charge transport pathways. Electrons migrate and hop between layers of the rod-like samples and between metal ions and ligands [52]. Moreover, free radicals within HHTP ligands further enhance conductive loss. At elevated frequencies, a clear transition from conductive to polarization loss is observed. More Cole–Cole semicircles indicate stronger polarization loss. Various polarization loss mechanisms exist in the samples, including defects polarization and dipole polarization. Dipole polarization plays a major role, resulting from the different electron donation and acceptance abilities of various bimetallic elements, leading to different dipolar polarizations and thus varying EMWA performances. Collectively, both conductive and polarization losses contribute substantially to the overall dielectric loss spectrum.

The conductivity measurements obtained by four-probe method (Table S2 in the ESM) revealed values of 1.67, 1.44, 0.39, 1.86, 1.91, and 1.95 S·m^{-1} for CuZn-1, CuZn-2, CuZn-3, CuMn-4, CuCo-5, and CuNi-6, respectively. These conductivity values stem from effective overlapping of the successful orbitals between the metal and the π-conjugated HHTP ligands, forming a continuous conductive network that enhances the conductivity loss. Consistent with the free electron theory ($\varepsilon'' = \sigma/(2\pi f\varepsilon_0)$), ε_0 represents the dielectric constant of the vacuum, the observed conductivity trends correlate well with the value of ε'' variations. It is worth noting that the conductivity of several samples is similar, indicating that the conductive loss gives the materials excellent dissipation of EMW, while it is the polarization loss that distinguishes the performance of the samples [11].

High-performance EMWA materials must simultaneously satisfy two key conditions: (1) high attenuation constant (α), (2) optimal impedance matching. The α can be expressed as Eq. (5) [7, 53]

$$\alpha = \frac{\sqrt{2}\pi f}{c}\sqrt{(\mu_r''\varepsilon_r'' - \mu_r'\varepsilon_r') + \sqrt{(\mu_r''\varepsilon_r'' - \mu_r'\varepsilon_r')^2 + (\mu_r'\varepsilon_r'' + \mu_r''\varepsilon_r')^2}} \quad (5)$$

The larger the α value, the greater the ability of the material to attenuate [3, 4]. The value of α is positively correlated with the imaginary components of the dielectric constants. As shown in Fig. 4(j), the α values for all samples exhibit an upward trend with increasing frequency, and the values rise from 30.81 to 171.22, 38.02 to 167.69, 23.03 to 93.58, 55.89 to 258.97, 48.93 to 307.11, and 59.61 to 280.58 m^{-1}, respectively. It is noteworthy that CuZn-1 exhibits significantly higher α values at 4.00–10.00 GHz com-pared to the other two CuZn-*X* samples, with a distinct peak observed between 6.00–10.00 GHz, where the α values is 238.61 m^{-1}, indicating excellent attenuation capability. This trend aligns consistently with the variation in ε'' values. Correspondingly, this sample demonstrates the best RL_{min} performance at 7.44 GHz. Correspondingly, as presented in Fig. 4(j) the α values of CuM-HHTP also exhibit an increasing trend, with the distinction that they are higher in comparison. An elevated α values enables the

material to achieve critical attenuation across broader frequency bands at reduced thicknesses. It is evident that impedance matching serves as an equally important criterion for evaluating EMWA materials. The supporting information contains the impedance matching equations. Figures 4(g)–4(i) and Fig. S6 in the ESM presents the impedance matching values for different samples. Excessively high conductivity may also lead to impedance mismatch [54]. When the value of impedance matching is below 0.4, more EMW can penetrate into the interior of the material without being emitted at its surface, thus indicating excellent EMWA characteristics [55]. Notably, Mn^{2+}, Co^{2+}, and Ni^{2+} incorporation substantially improves the impedance matching capability of these samples, though this effect diminishes less pronounced at higher conductivity levels. The broad EAB achieved by CuZn-2, CuMn-4, CuCo-5, and CuNi-6 at ultrathin thicknesses results from an optimal balance between attenuation capability and impedance matching. Therefore, achieving a productive balance between impedance matching and attenuation is essential for outgoing EAB applications. Notably, the equivalent CuNi-6 sample exhibits an appropriate impedance matching range and an excellent α value, accounting for its widest EAB range of 7.12 GHz.

Our systematic analysis reveals the EAB value increases with the enhanced electron donation and acceptance abilities of the elemental ions. This correlation stems from intensified electron transfer capability between the metals and the functional groups of the ligands as the electron transfer abilities increase, resulting in a greater dipolar polarization intensity, which promotes EMWA. Furthermore, the EAB value is related to the balance between attenuation and impedance matching. In this study, we achieved a record EAB value of 7.12 GHz at merely 1.78 mm in CuNi-6 demonstrating the efficacy of bimetallic composition engineering.

Figure 4(k) summarizes the optimal EAB performance and their corresponding thicknesses for all sample, enabling clear cross-comparison. Notably, the CuNi-6 stands out with an industry-leading EAB of 7.12 GHz at just 1.78 mm. When benchmarked against (Fig. S7 in the ESM) recently reported EMWA materials, our EAB and matched thicknesses and thickness metrics demonstrate superior performance [56–62]. Notably, conductive MOFs developed in this work achieve ultrawide bandwidth coupled with strong absorption at ultrathin thicknesses, establishing them as next-generation MOFs for advanced EMWA applications.

As summarized in Fig. 5(a), the EMWA mechanism operates through multiple synergistic effects. The porous structure is advantageous to balance the impedance matching. Furthermore, the well-defined structure induces multiple scattering and reflections of the EMW entering the sample [57, 63]. Additionally, strong π–π conjugate interactions within the sample form a π-conjugate conducting network, significantly enhancing conductivity loss [12]. Especially, metal ions and organic ligands consecutively form delocalized conductive MOFs with matched energy levels and overlapping orbitals, promoting efficient charge transfer [30]. The bimetallic composition introduces multiple polarization loss mechanisms, including interface polarization, defects polarization, and dipole polarization, which all contribute to EMWA [2, 10, 23]. Particularly, the dipole polarization caused by the interaction between the metals and the functional groups of the organic ligands

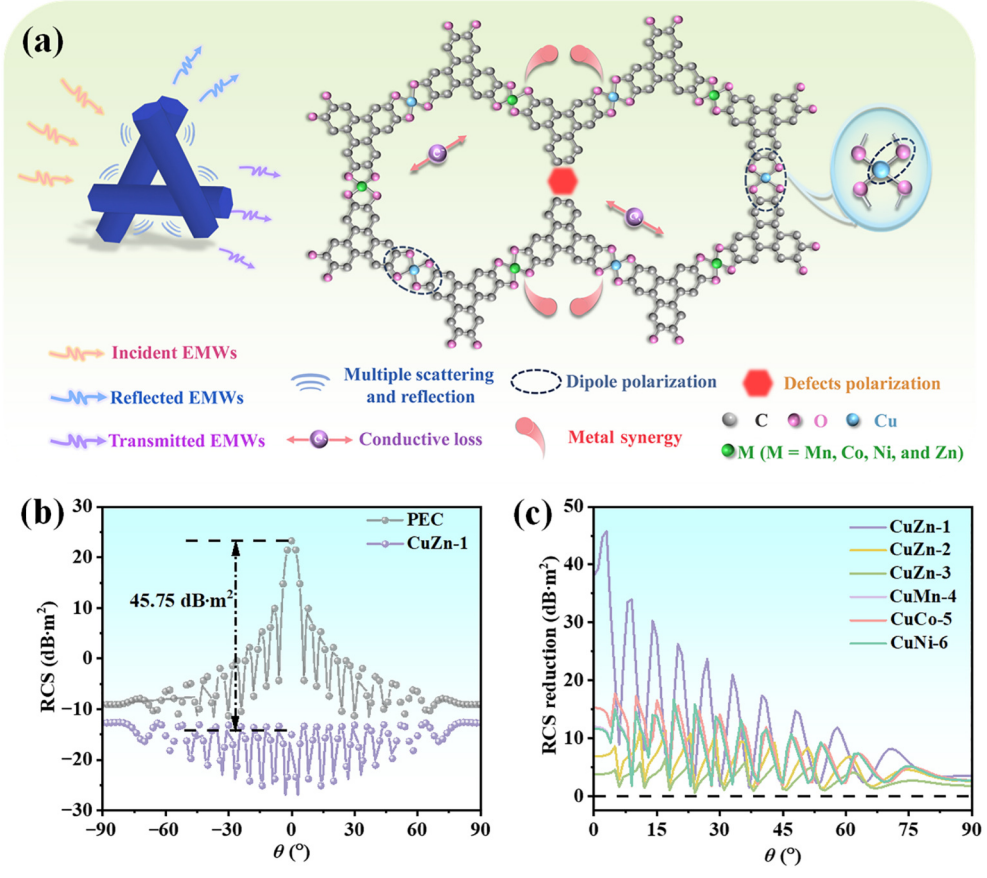

Figure 5 (a) Schematic illustration of the EMWA mechanisms for CuM-HHTP (M = Mn, Co, Ni, and Zn) nano-materials. (b) Simulated RCS values of the CuZn-1 under certain detecting angles. (c) RCS reduction values of all samples.

improves the polarization loss [8, 23, 57]. In summary, the combined effect of the rod-like morphology and internal optimized structure collectively enable efficient EMW energy dissipation.

To assess real-world applicability, we conducted radar cross-section (RCS) distributions using computer simulation technology (CST) Microwave Studio, quantifying the samples' electromagnetic stealth capabilities. The scattering direction of the RCS value (σ) for a specific scattering source was determined by the spherical coordinates θ and φ. The RCS distribution images, shown in Fig. S8 in the ESM, illustrate the reflected signals from models of metal substrates coated with various materials. Notably, the configuration featuring a CuZn-1 coating on the PEC substrate exhibited the lowest vertical radar scattering intensity, indicating excellent electromagnetic energy absorption capabilities [64]. The corresponding 1D RCS curves (Figs. 5(b) and 5(c)) further emphasized the outstanding EMWA performance of CuZn-1 at all angles, achieving an impressive RCS reduction of 45.75 dB·m^2. These simulation results demonstrate that CuZn-1 exhibits outstanding potential for practical EMW attenuation applications, with particular effectiveness in minimizing EMW scattering and reducing electromagnetic reflection.

4 Conclusions

A series of the CuM-HHTP materials were synthesized via a one-step hydrothermal method. The electron transfer capability of the metal ions (Ni > Co > Zn > Mn) was found to positively correlate with EAB value at ultrathin thicknesses. Notably, the CuNi-6 exhibited an exceptionally wide EAB value of 7.12 GHz (10.88–18.00 GHz) at a minimal thickness of only 1.78 mm. The outstanding performance was attributed to the impedance matching, dipole polarization, defect-induced polarization, interface polarization, and conductive loss. Consequently, this work provides a novel strategy for designing high-performance bimetallic conductive MOF-based absorbers.

Electronic Supplementary Material: Supplementary material (experimental details, additional measurements, and additional theoretical results) is available in the online version of this article at https://doi.org/10.26599/NR.2025.94907919.

Data availability

All data needed to support the conclusions in the paper are presented in the manuscript and the Electronic Supplementary Material. Additional data related to this paper may be requested from the corresponding author upon request.

Acknowledgements

This work was financially supported by the National Natural Science Foundation of China (Nos. 52173267, 21667019, and 22066017), Postgraduate Research & Practice Innovation Program of Jiangsu Province (Nos. SJCX23_XY009 and KYCX24_XZ001), and the key laboratory of high temperature electromagnetic materials and structure of MOE (No. KB202402).

Declaration of competing interest

All the contributing authors reports no conflict of interests in this work.

Author contribution statement

W. Q. Z.: Writing – original draft, visualization, investigation, formal analysis, data curation. J. H. L.: Conceptualization, funding acquisition, project administration, writing – review & editing. J. H. S.: Formal analysis, investigation. B. J. H.: Investigation. X. C. L.: Resources, writing – review & editing. Y. X.: Writing – review & editing.

Use of AI statement

None.

References

[1] Huang, M. Q.; Li, B. X.; Qian, Y. T.; Wang, L.; Zhang, H. B.; Yang, C. D.; Rao, L. J.; Zhou, G.; Liang, C. Y.; Che, R. C. MOFs-derived strategy and ternary alloys regulation in flower-like magnetic-carbon microspheres with broadband electromagnetic wave absorption. *Nano-Micro Lett.* **2024**, *16*, 245.

[2] Liu, J. L.; Zhang, S. Y.; Qu, D.; Zhou, X. J.; Yin, M. X.; Wang, C. X.; Zhang, X. L.; Li, S. C.; Zhang, P. J.; Zhou, Y. Q. et al. Defects-rich heterostructures trigger strong polarization coupling in sulfides/carbon composites with robust electromagnetic wave absorption. *Nano-Micro Lett.* **2025**, *17*, 24.

[3] Qiu, Z. R.; Liu, X. Y.; Yang, T. Y.; Wang, J. B.; Wang, Y.; Ma, W. L.; Huang, Y. Synergistic enhancement of electromagnetic wave absorption and corrosion resistance properties of high entropy alloy through lattice distortion engineering. *Adv. Funct. Mater.* **2024**, *34*, 2400220.

[4] Wen, J. M.; Liu, Y. Y.; Hui, S. C.; Deng, L. C.; Zhang, L. M.; Fan, X. M.; Chen, Q.; Liu, X. M.; Li, X. C.; Yan, N. et al. Lattice compressive strain-controlled electromagnetic wave absorption in TMDs by plasma-assisted rapid annealing. *Matter* **2025**, *8*, 102151.

[5] Shao, G. F.; Xu, R. P.; Chen, Y.; Yu, G. Y.; Wu, X. D.; Quan, B.; Shen, X. D.; Huang, X. G. Miniaturized hard carbon nanofiber aerogels: From multiscale electromagnetic response manipulation to integrated multifunctional absorbers. *Adv. Funct. Mater.* **2024**, *34*, 2408252.

[6] Sun, C. H.; Lan, D.; Jia, Z. R.; Gao, Z. G.; Wu, G. L. Kirkendall effect-induced ternary heterointerfaces engineering for high polarization loss MOF-LDH-MXene absorbers. *Small* **2024**, *20*, 2405874.

[7] Liu, J. C.; Xu, L. Y.; Shao, C.; Liu, Z. L.; Zhang, G. W.; Guan, Y. A.; Zhang, Y. Y.; Lei, X. Y.; Dai, Y.; Zhao, W. et al. Synergistic dielectric and magnetic effects boosting electromagnetic wave absorption in Flower-Ball-like VSe_2@$CoFe_2O_4$ composites. *Chem. Eng. J.* **2024**, *499*, 156244.

[8] Wei, C. H.; Shi, L. Z.; Li, M. Q.; He, M. K.; Li, M. J.; Jing, X. R.; Liu, P. B.; Gu, J. W. Hollow engineering of sandwich NC@Co/NC@MnO_2 composites toward strong wideband electromagnetic wave attenuation. *J. Mater. Sci. Technol.* **2024**, *175*, 194–203.

[9] Zhang, K. L.; Liu, Y. H.; Liu, Y. N.; Yan, Y. F.; Ma, G. S.; Zhong, B.; Che, R. C.; Huang, X. X. Tracking regulatory mechanism of trace Fe on graphene electromagnetic wave absorption. *Nano-Micro Lett.* **2024**, *16*, 66.

[10] Li, Z. C.; Liang, J.; Wei, Z. H.; Cao, X.; Shan, J. H.; Li, C. W.; Chen, X. Y.; Zhou, D.; Xing, R. Z.; Luo, C. J. et al. Lightweight foam-like nitrogen-doped carbon nanotube complex achieving highly efficient electromagnetic wave absorption. *J. Mater. Sci. Technol.* **2024**, *168*, 114–123.

[11] Hui, S. C.; Chen, Q.; Tao, K.; Zhang, L. M.; Fan, X. M.; Che, R. C.; Wu, H. J. Highly mixed index facet engineering induces defect formation and converts the wave-transmissive Mott insulator NiO into electromagnetic wave absorbent. *Adv. Mater.* **2025**, *37*, 2415844.

[12] Shan, Z.; Cheng, S. Y.; Wu, F.; Pan, X. H.; Li, W. J.; Dong, W.; Xie, A. M.; Zhang, G. Electrically conductive Two-dimensional Metal-Organic frameworks for superior electromagnetic wave absorption. *Chem. Eng. J.* **2022**, *446*, 137409.
[13] Chen, X.; Li, M. X.; Yan, J. L.; Zhang, L. L. MOF-derived nanocarbon materials for electrochemical catalysis and their advanced characterization. *New Carbon Mater.* **2024**, *39*, 78–99.
[14] Yin, Q. Y.; Xu, T.; Cao, F. H.; Wang, Y. Y.; Yang, C.; Liu, N.; Liu, J.; Liu, R. M. Heterostructures of NiFe-MOF/PBAs with high-performance supercapacitors obtained by compounding Prussian blue analogues on bimetallic organic frames. *Electrochim. Acta* **2024**, *476*, 143749.
[15] Shahzad, U.; Marwani, H. M.; Saeed, M.; Asiri, A. M.; Althomali, R. H.; Rahman, M. M. Exploration of porous metal-organic frameworks (MOFs) for an efficient energy storage applications. *J. Energy Storage* **2023**, *74*, 109518.
[16] Wang, J.; Xu, Q. B.; Yang, Y.; Liu, J. X.; Kong, W. J.; Shi, L. C. An electrochemical sensor founded on heterogeneous MXene & MOF composite for tanshinol sensing. *Talanta* **2024**, *268*, 125344.
[17] Ban, Q. F.; Li, L. W.; Liu, H. M.; Zhou, D.; Zheng, Y. C.; Qin, Y. S.; Xing, R. Z.; Kong, J. Polymerization-induced assembly-etching engineering to hollow Co@N-doped carbon microcages for superior electromagnetic wave absorption. *Carbon* **2023**, *215*, 118506.
[18] Wang, Y. C.; Haidry, A. A.; Liu, Y. J.; Raza, A.; Duan, L. T.; He, C.; Zhou, J. T. Enhanced electromagnetic wave absorption using bimetallic MOFs-derived TiO_2/Co/C heterostructures. *Carbon* **2024**, *216*, 118497.
[19] Zhang, W.; Tan, G. G.; Hu, J. X.; Wang, Q. W.; Yan, W. R.; Man, Q. K. Enhancing electromagnetic wave absorption performance through co-regulation of microstructure and spatial orientation of RE–Ni MOF. *Chem. Eng. J.* **2023**, *478*, 147414.
[20] Wang, H. H.; Cui, X.; Gao, Z. A.; Shi, H. C.; Liu, F. Z. NiCo–MOF composed of small fragments were multi-dimensional reinforced with conductive polyaniline for high performance supercapacitors. *J. Phys. Chem. Solids* **2024**, *187*, 111876.
[21] Jiang, W. H.; Qian, H. Q.; Cao, Q. Y.; Jiang, B. Recyclable flexible materials with MOF-derived nanospheres for electromagnetic wave absorption. *Compos. Commun.* **2024**, *46*, 101829.
[22] Tu, Z. X.; Zhang, G. Y.; Liao, L. L.; Wang, H. M. Theoretical screening and experimental validation of M_3(2,3,6,7,10,11-hexahydroxytriphenylene)$_2$ for electrocatalytic CO_2 reduction. *Mol. Catal.* **2023**, *540*, 113033.
[23] Chen, C. J.; Shan, Z.; Tao, S. F.; Xie, A. M.; Yang, H. W.; Su, J.; Horke, S.; Kitagawa, S.; Zhang, G. Atomic tuning in electrically conducting bimetallic organic frameworks for controllable electromagnetic wave absorption. *Adv. Funct. Mater.* **2023**, *33*, 2305082.
[24] Zhang, G. X.; Jin, L.; Zhang, R. X.; Bai, Y.; Zhu, R. M.; Pang, H. Recent advances in the development of electronically and ionically conductive metal-organic frameworks. *Coord. Chem. Rev.* **2021**, *439*, 213915.
[25] Li, J. R.; Huang, Y. Q.; Zhou, Y. L.; Dong, H.; Wang, H. Y.; Shan, H. R.; Li, Y. F.; Xu, M. T.; Wang, X. B. Controllable construction of two-dimensional conductive M_3(HHTP)$_2$ nanorods for electrochemical sensing of malachite green in fish. *ACS Appl. Nano Mater.* **2023**, *24*, 22916–22926.
[26] Qu, N.; Xu, G. X.; Liu, Y. K.; He, M. K.; Xing, R. Z.; Gu, J. W.; Kong, J. Multi-scale design of metal-organic framework metamaterials for broad-band microwave absorption. *Adv. Funct. Mater.* **2025**, *35*, 2402923.
[27] Liu, K. K.; Meng, Z.; Fang, Y.; Jiang, H. L. Conductive MOFs for electrocatalysis and electrochemical sensor. *eScience* **2023**, *3*, 100133.
[28] Iqbal, M. Z.; Shaheen, M.; Khan, M. W.; Siddique, S.; Farid, S.; Aftab, S.; Wabaidur, S. M. The rise of 2D conductive metal-organic framework: Cu_3(HHTP)$_2$ d-π MOF for integrated battery-supercapacitor hybrids. *Mater. Today Sustain.* **2023**, *22*, 100331.
[29] Wu, L. Q.; Li, W. J.; Yin, Y. T.; Liu, Z.; Zheng, B.; Zhang, Q. Y.; Hao, Z. D. *In-situ* construction of $Ti_3C_2T_X$/Ni–HHTP heterostructure as anode for lithium-ion batteries. *Mater. Today Commun.* **2024**, *38*, 108160.
[30] Guo, L. Z.; Sun, J. F.; Sun, X.; Zhang, J. Y.; Hou, L. R.; Yuan, C. Z. Construction of 1D conductive Ni–MOF nanorods with fast Li^+ kinetic diffusion and stable high-rate capacities as an anode for lithium ion batteries. *Nanoscale Adv.* **2019**, *1*, 4688–4691.
[31] Li, X. X.; Li, J. J.; Kurbanjan, D.; Yu, T. H.; Du, H. Synergistic effect of trimetallic doping and π-π conjugation in NiZnCo–ZIF@HHTP for efficient oxygen evolution reaction. *J. Electroanal. Chem.* **2023**, *937*, 117410.
[32] Yin, X. J.; Li, Y. M.; Cai, W. S.; Fan, C.; Liu, W. Q.; Wang, N. N.; Qin, G. X.; Xie, Z.; Chen, X. D.; Han, Y. *In-situ* synthesis of Cu-based conductive metal organic frameworks on graphene layers for high-performance lithium and potassium ion batteries. *Appl. Surf. Sci.* **2023**, *624*, 157124.
[33] Wang, L. C.; Pan, L. Y.; Han, X.; Ha, M. N.; Li, K. R.; Yu, H.; Zhang, Q. H.; Li, Y. G.; Hou, C. Y.; Wang, H. Z. A portable ascorbic acid in sweat analysis system based on highly crystalline conductive nickel-based metal-organic framework (Ni-MOF). *J. Colloid Interface Sci.* **2022**, *616*, 326–337.
[34] Luo, C. J.; Wang, Y.; Hu, X.; Wu, Y. F.; Wang, Y.; Chao, M.; Yan, L. K. High temperature stable amorphous SiBCN microwave absorption ceramics derived from one-pot synthesis of single-source precursors. *Mater. Res. Bull.* **2024**, *174*, 112718.
[35] Li, J. H.; Wei, Y. Z.; Huang, M. Q.; Gao, W. T.; Yao, K.; Ma, H. F. Dually inner-porous composites with Co@C prismatic rods anchored into graphene aerogel toward superior electromagnetic wave absorbing materials. *J. Alloy. Compd.* **2024**, *970*, 172449.
[36] Qiao, J.; Zhang, X.; Liu, C.; Zeng, Z. H.; Yang, Y. F.; Wu, L. L.; Wang, F. L.; Wang, Z.; Liu, W.; Liu, J. R. Facile synthesis of MnS nanoparticle embedded porous carbon nanocomposite fibers for broadband electromagnetic wave absorption. *Carbon* **2022**, *191*, 525–534.
[37] Zhang, Y.; Liu, X. H.; Guo, Z. Q.; Jia, C. Y.; Lu, F.; Jia, Z. R.; Wu, G. L. MXene@Co hollow spheres structure boosts interfacial polarization for broadband electromagnetic wave absorption. *J. Mater. Sci. Technol.* **2024**, *176*, 167–175.
[38] Zhang, Z. Y.; Gao, T.; Zhao, R. Z.; Hu, C. L.; Liao, Y. J.; Liu, X. L.; Zhang, Z. H.; Li, Y. X.; Zhang, X. F. High easy-plane anisotropy Y–Co intermetallic nanoparticles for boosting gigahertz magnetic loss ability. *Acta Mater.* **2024**, *272*, 119947.
[39] Li, Q. Y.; Liu, L. Y.; Kimura, H.; Zhang, X. Y.; Liu, X. Y.; Xie, X. B.; Sun, X. Q.; Xu, C. Y.; Du, W.; Hou, C. X. Restricted growth of molybdenum carbide nanoparticles in hierarchically porous nitrogen-doped carbon matrix for boosting electromagnetic wave absorption performance. *J. Colloid Interface Sci.* **2024**, *655*, 634–642.
[40] Guo, X. L.; Wang, H.; Xing, P. F.; Wang, S.; Jiang, S. N.; Zhuang, Y. X. Organosilane waste-derived SiCnws/SiOC composites with enhanced electromagnetic wave absorption performance. *Ceram. Int.* **2024**, *50*, 8269–8276.
[41] Bonchev, D. Information theory interpretation of the Pauli principle and Hund rule. *Int. J. Quantum Chem.* **1981**, *19*, 673–679.
[42] Mai, C. W.; Huang, N. N.; Gao, M. Y.; Sun, Y. S.; Yan, J. F.; Zhai, C. X.; Zhao, W. Natural green raw-based Biochar@Co/C composites: Simple water bath synthesis and excellent electromagnetic wave absorption properties. *J. Alloy. Compd.* **2023**, *968*, 171960.
[43] Wang, S. J.; Zhang, X.; Tang, Y. X.; Hao, S. Y.; Zheng, S. N.; Qiao, J.; Wang, Z.; Wu, L. L.; Liu, J. R.; Wang, F. L. Facile fabrication of biomass chitosan-derived magnetic carbon aerogels as multifunctional and high-efficiency electromagnetic wave absorption materials. *Carbon* **2024**, *216*, 118528.
[44] Zhao, X. X.; Huang, Y.; Liu, X. D.; Jiang, H. Y.; Yu, M.; Ma, X. F.;

Zong, M.; Liu, P. B. Hollow multi-layer bowknot like nanoparticles surface modified by TMDs derived flexible fiber membranes for electromagnetic wave absorption. *Chem. Eng. J.* **2024**, *483*, 149085.

[45] Nie, Z. G.; Feng, Y.; Hu, X. M.; Su, J.; Zhao, Z. Y.; Chen, J. Q.; Wang, R. M.; Qi, S. H. *In situ*-growth ultrathin hexagonal boron nitride /N-doped reduced graphene oxide composite aerogel for high performance of thermal insulation and electromagnetic wave absorption. *Ceram. Int.* **2023**, *49*, 36080–36091.

[46] Chen, Z. L.; Zhang, J. H.; Ni, L. Y.; Sheng, D. H.; Gao, R. R.; Li, W. J.; Xie, A. M. Improving electromagnetic wave absorption property of metal borides/carbon nanocomposites by magnetic-electric balance and ion substitution tuning strategy. *Carbon* **2024**, *221*, 118901.

[47] Li, F. S.; Li, Q. Y.; Kimura, H.; Xie, X. B.; Zhang, X. Y.; Wu, N. N.; Sun, X. Q.; Xu, B. B.; Algadi, H.; Pashameah, R. A. et al. Morphology controllable urchin-shaped bimetallic nickel-cobalt oxide/carbon composites with enhanced electromagnetic wave absorption performance. *J. Mater. Sci. Technol.* **2023**, *148*, 250–259.

[48] Huang, X. B.; Wang, Y. T.; Lou, Z. C.; Chen, Y. X.; Li, Y. J.; Lv, H. L. Porous, magnetic carbon derived from bamboo for microwave absorption. *Carbon* **2023**, *209*, 118005.

[49] Xu, Z. H.; Huang, J. G.; Xiong, K. W.; Sun, M. Z.; Ji, J. C.; Cao, Z. J. Tailoring electromagnetic wave absorption using *in-situ* precipitation of $BaTiO_3$–$BaFe_{12}O_{19}$ glass ceramic. *Ceram. Int.* **2024**, *50*, 3119–3128.

[50] Wang, J. L.; Yin, T.; Zhang, C.; Yang, W.; Jiang, B.; Li, Y. F.; Xu, C. M. The synthesis of porous carbon material derived from coal liquefied residue and its electromagnetic wave absorption. *New Carbon Mater.* **2023**, *38*, 875–886.

[51] Sun, Z. X.; Shen, J. H.; Chen, Y. M.; Jiang, S. H.; Zhou, L. J.; Li, X. P.; Zheng, J. J. Multi-scale heterostructures of MXene-based composites for adjustable electromagnetic wave absorption. *J. Alloy. Compd.* **2024**, *976*, 173253.

[52] Iqbal, M. Z.; Shaheen, M.; Khan, M. W.; Siddique, S.; Farid, S.; Aftab, S.; Wabaidur, S. M. Elucidating d- conjugated two-dimensional 2,3,6,7,10,11-hexahydroxytriphenylene based conductive metal-organic framework for hybrid supercapacitors. *Electroanal. Chem.* **2023**, *943*, 117564.

[53] Li, X. G.; Yan, H. T.; He, C. H.; Wei, W.; Fan, F. L.; Shi, Z. Q.; Dan, J. M.; Wen, X. D.; Lv, Y. Synthesis of double-shell carbonyl iron powder @SiO_2 @C for enhanced electromagnetic wave absorption. *J. Alloy. Compd.* **2024**, *976*, 173233.

[54] Xu, H. Y.; Liu, M. J.; Ma, Z.; Kang, B.; Zhang, X.; Zhu, C. L.; Zhang, X. T.; Chen, Y. J. Zn,N-codoped mesoporous carbon particles/carbon fibers for wide-band electromagnetic wave absorption. *Chem. Eng. J.* **2024**, *479*, 147666.

[55] Zhao, Q. X.; Li, X. Y.; Zhang, C.; Ma, B. C.; Jia, D. J.; Chigan, T. L.; Yang, P. P. Preparation of NiS/$Ti_3C_2T_x$ co-doped with N and P at the covalent interface and its electromagnetic wave absorption properties. *J. Colloid Interface Sci.* **2023**, *652*, 1250–1260.

[56] Zhu, H. H.; Jiao, Q. Z.; Fu, R. R.; Su, P. J.; Yang, C.; Feng, C. H.; Li, H. S.; Shi, D. X.; Zhao, Y. Cu/NC@Co/NC composites derived from core–shell Cu-MOF@Co-MOF and their electromagnetic wave absorption properties. *J. Colloid Interface Sci.* **2022**, *613*, 182–193.

[57] Zhang, X.; Tian, X. L.; Qin, Y. T.; Qiao, J.; Pan, F.; Wu, N.; Wang, C. X.; Zhao, S. Y.; Liu, W.; Cui, J. et al. Conductive metal-organic frameworks with tunable dielectric properties for boosting electromagnetic wave absorption. *ACS Nano* **2023**, *17*, 12510–12518.

[58] Zhong, W. X.; Li, B.; Ma, Z.; Zhu, C. L.; Yan, F.; Zhang, X. T.; Chen, Y. J. Double salt-template strategy for the growth of N, S-codoped graphitic carbon nanoframes on the graphene toward high-performance electromagnetic wave absorption. *Carbon* **2023**, *202*, 235–243.

[59] Zhao, H. T.; Wang, Q. J.; Ma, H. L.; Zhao, Y.; Li, L.; Li, P. B.; Yan, J. F.; Yun, J. N.; Zhao, W.; Zhang, H. et al. Hollow spherical NiFe-MOF derivative and N-doped rGO composites towards the tunable wideband electromagnetic wave absorption: Experimental and theoretical study. *Carbon* **2023**, *201*, 347–361.

[60] Shu, Y.; Zhao, T. K.; Li, X. H.; Yang, L.; Cao, S. Q.; Ahmad, A.; Jiang, T.; Luo, H. J.; Jing, Z. M.; Ui Ain, N. Surface plasmon resonance-enhanced dielectric polarization endows coral-like Co@CoO nanostructures with good electromagnetic wave absorption performance. *Appl. Surf. Sci.* **2022**, *585*, 152704.

[61] Zhang, Y. H.; Li, Y.; Liu, H. J.; Zhang, L.; Zhang, Y.; Xu, C. C.; Gong, C. H. Biomass-derived heterogeneous RGO/Ni/C composite with hollow structure for high-efficiency electromagnetic wave absorption. *Mater. Today Phys.* **2023**, *31*, 100966.

[62] Hou, W. X.; Peng, K.; Li, S. K.; Huang, F. Z.; Wang, B. J.; Yu, X. Y.; Yang, H. X.; Zhang, H. Designing flower-like MOFs-derived N-doped carbon nanotubes encapsulated magnetic NiCo composites with multi-heterointerfaces for efficient electromagnetic wave absorption. *J. Colloid Interface Sci.* **2023**, *646*, 265–274.

[63] Liu, Y.; Zeng, Z. H.; Zheng, S. N.; Qiao, J.; Liu, W.; Wu, L. L.; Liu, J. R. Facile manufacturing of Ni/MnO nanoparticle embedded carbon nanocomposite fibers for electromagnetic wave absorption. *Compos. Part B: Eng.* **2022**, *235*, 109800.

[64] Feng, Z. B.; Liu, C. B.; Li, X.; Luo, G. S.; Zhai, N. X.; Hu, R. Z.; Lin, J.; Peng, J. B.; Peng, Y. H.; Che, R. C. Designing electronic structures of multiscale helical converters for tailored ultrabroad electromagnetic absorption. *Nano-Micro Lett.* **2025**, *17*, 20.